7-2020

All-Metallic Phase Change Thermal Management Systems for Transient Spacecraft Loads

Carl R. Hartsfield
Air Force Institute of Technology

Travis Shelton

Brian O. Palmer

Ryan P. O'Hara

Recommended Citation

Hartsfield, C. R., Shelton, T. E., Palmer, B. O., & O'Hara, R. (2020). All-Metallic Phase Change Thermal Management Systems for Transient Spacecraft Loads. Journal of Aerospace Engineering, 33(4), 04020039. https://doi.org/10.1061/(ASCE)AS.1943-5525.0001150

ASCE

All-Metallic Phase Change Thermal Management Systems for Transient Spacecraft Loads

Carl R. Hartsfield[1]; Travis E. Shelton[2]; Brian O. Palmer[3]; and Ryan O'Hara[4]

Abstract: In this work, we explore the thermal properties of gallium as an effective phase change material for thermal management applications. Thermal storage and dissipation of gallium manufactured heat sinks were compared to conventional phase change heat sinks. The comparison revealed a 50-fold (80 K versus 1.5 K) potential reduction in temperature during the phase change process due to the high density, thermal conductivity, and latent heat of fusion. The gallium creates shallow thermal gradients when transiently heated, producing a nearly isothermal process. Computational estimates using lumped sum parameters were able to provide simple modeling to predict the results. Gallium based phase change devices offer a combination of low volume, small temperature drops across the device, simplicity of manufacture and design, and high energy storage applications. **DOI: 10.1061/(ASCE)AS.1943-5525.0001150.**

Introduction

High peak power, low-duty cycle electronics, such as communication systems on spacecraft, require careful thermal management to avoid losses in reliability due to overheating. Thermal management systems for a space environment create unique design challenges. First, no mechanisms are present other than thermal radiation to transfer energy into or out of the system. Operation in the vacuum of space, while continuously moving several km/s, negates the potential for either conductive or convective means of energy transfer. Second, for most Earth-orbiting spacecraft, the thermal radiation environment is constantly changing. Satellites go into and out of eclipse conditions regularly, with satellites in low Earth orbit (LEO) experiencing cycles as quickly as once every 86.5 min (Agrawal 1986). Lastly, a spacecraft in LEO, achieves an average line of sight (LOS) radio communication link with their ground stations for a few minutes (<8 min) per an orbital pass due to the brief transmitting or receiving times. In particular, radio frequency (RF) amplifiers are used as part of the radio communications system, requiring the satellite to have both high input power requirements while operating at low efficiency. These factors result in most of the power turning into heat on the spacecraft that must be dissipated (Wertz et al. 2011).

Thermal issues become more sensitive in a smaller spacecraft, especially nanosatellites (1–10 kg) and microsatellites (10–100 kg) (Defense Industry Daily Staff 2011). One specific category of nano- or microsatellite is the CubeSat, defined in terms of units (U) of volume. These satellites become thermally dense, due to the small volume ($10 \times 10 \times 10$ cm) and mass (1.5–2 kg) per U. In all cases, surface area is limited and thus, thermal dissipation via radiation becomes restricted due to the small geometry and necessary accommodations for other subsystems at the structure's surface, including apertures, sun sensors, Earth sensors, star trackers, photovoltaic cells, and communication antennas. As an example, a $12U$ CubeSat might have a total of 0.32 m^2 of surface area, but less than 25% of that total might be available for thermal radiators (Agrawal 1986). Radiator area is directly related to the amount of heat to be rejected, and the temperature threshold at which it is to be removed. The relationship is described by the Stefan-Boltzmann equation

$$Q = \varepsilon \sigma A (T_{surf}^4 - T_\infty^4) \tag{1}$$

where the total heat to be removed Q (in W), is proportional to the emissivity ε, the Stefan-Boltzmann constant $\sigma = 5.67 \times 10^{-8}$ W/m · K, the surface area A (in m^2), and the difference between surface temperature (T_{surf}) to the fourth power and environment temperature (T_∞) to the fourth power. Most space applications can treat the environmental temperature as the deep-space solid hydrogen temperature (~4 K). In this case, the impact of environmental temperature on the heat rejection capability of a radiator can effectively be ignored. If there is significant interaction with the Earth (large view factors to the Earth's surface), this will become more complex. However, for simple cases and relatively high emissivity ($\varepsilon \geq 0.9$), the heat rejection is approximately 430 W/m^2 at 30°C and 550 W/m^2 at 50°C (Agrawal 1986).

For example, we consider a nominal radio consuming 10 W of electricity, in which 1 W was transmitted as RF power, leaving 9 W generating heat. In all cases, the heat must be conducted through a structure from the electronics to the radiator, resulting in the electronics operating at a considerably higher temperature than the radiator (Bergman et al. 2011). Real time radiation would require a 15×15 cm radiator at 30°C or a 13×13 cm radiator at 50°C. Since these are both beyond the 10×10 cm single side of a $1U$ CubeSat component, they may be too large for the design space. To dissipate 9 W of heat, steady state, from a 10×10 cm area would require the radiator to operate at 91°C. Keeping the operating temperatures of electronics low is critical to their reliable operation over time. Raising the radiator temperature by 60°C (from 30°C to 90°C) will dramatically reduce the life of the radio.

[1]Assistant Professor, Air Force Institute of Technology, 2950 Hobson Way, Wright Patterson AFB, OH 45433 (corresponding author). ORCID: https://orcid.org/0000-0002-6224-7127. Email: carl.hartsfield@afit.edu

[2]Research Engineer, Air Force Institute of Technology, 2950 Hobson Way, Wright Patterson AFB, OH 45433. Email: travis.shelton@afit.edu

[3]M.S. Student, Air Force Institute of Technology, 2950 Hobson Way, Wright Patterson AFB, OH 45433. Email: brian.palmer.9@us.af.mil

[4]Assistant Professor, Air Force Institute of Technology, 2950 Hobson Way, Wright Patterson AFB, OH 45433. Email: sales@ohararp.com

Note. This manuscript was submitted on September 18, 2019; approved on February 5, 2020; published online on May 8, 2020. Discussion period open until October 8, 2020; separate discussions must be submitted for individual papers. This paper is part of the ***Journal of Aerospace Engineering***, © ASCE, ISSN 0893-1321.

Temperature Impact on Spacecraft Reliability

Reliability and expected lifetime of electronic components can be understood by the following analysis: MIL-HDBK-217F *Reliability Prediction of Electronic Equipment* (Department of Defense 1991). MIL-HDBK-217F is a reliability analysis that breaks down electronics into components for individual evaluation. Then, an overall assessment of the assembly's reliability is produced. For purposes of this study, the transceiver radio was estimated to consist of 37 integrated circuit semiconductor devices and 17 amplifier transistors. These values were based on common radios and should not be considered for in-depth analysis. Case and junction temperatures were assumed to be similar in all components. The 37 semiconductor devices were all modeled the same way, metal-oxide semiconductor devices (MOS) using microprocessor failure rate constants. The general equation for failure rate is

$$\lambda_p = (C_1\pi_T + C_2\pi_E)\pi_Q\pi_L \qquad \text{Failures}/10^6 \text{ h} \tag{2}$$

Table 1 contains a more complete explanation of the variables and the values used in calculated estimated failure rates for semiconductor processor devices in this case.

When evaluating the impact of multiple devices, the device failure rate is the summation of each device

$$\lambda_{p,total} = \sum_{all} \lambda_p \tag{3}$$

This model assumes device failure results in a system failure. If redundant strings are implemented, the formulation would be different, but redundancy is not incorporated into this model. The 17 power amplifier transistors were modeled as similar devices using the following equation and inputs:

$$\lambda_p = \lambda_b\pi_T\pi_A\pi_M\pi_Q\pi_E \qquad \text{Failures}/10^6 \text{ h} \tag{4}$$

Table 2 contains an explanation of these variables and the values used in calculating failure rates for RF amplifiers in this model.

From a known case temperature, the junction temperature within the electronics can be estimated and used to calculate the failure rate per million hours of service. A typical satellite system level reliability requirement will be utilized for the individual subsystems. At minimum, this will include attitude determination and control systems (ADCS), telemetry tracking and control (TT&C), command and data handling (C&DH), propulsion, and electrical power system (EPS). For the purposes of this research, the system reliability was considered to be equally allocated to these five subsystems (Wertz et al. 2011). Therefore, the subsystem reliability is the fifth root of the required reliability (Department of Defense 1991). Eq. (5) can be used to estimate system life (t_{life}) for the system

$$t_{life} = \frac{-\ln(r)}{\sum_i n_i\lambda_{p,i}} \tag{5}$$

The estimated life of the electronics, for example a modeled radio transceiver, is shown in Fig. 1. A 5°C case temperature increase results in a 10%–17% decrease in mission life, across all reliability requirement assumptions. The general trend of a rapid decrease in mission life with increasing temperature is broadly applicable, and serves as the motivation for this research. Efforts to minimize case temperature variations and absolute temperatures will result in increased reliability and service life.

High Thermal Capacity Materials

As low temperature real time dissipation of the heat is limited, two options including a high thermal capacity to store thermal energy or a phase change system are considerations. First, a material of high thermal conductivity and thermal capacity can be utilized for the mass. Conservation of energy [Eq. (6)], determines the fundamental thermal transport when assuming lumped parameter behavior and neglecting temperature distribution within the heat sink. As heat is applied to the heat sink in the form of continued radio

Table 1. Description of variables for Eq. (2)

Variable	Value	Description
C_1	0.28	Die complexity, assumes 16 bit
C_2	$0.004663 = 0.00003 \cdot (\#pins)^{1.82}$	Package failure rate, 16 pin, flatpack
π_T	$0.1\exp\left(\frac{-0.035}{8.617\cdot 10^{-5}}\left(\frac{1}{T_J+273}-\frac{1}{296}\right)\right)$	Temperature factor
		T_j: junction temperature, T_c: case temperature (°C)
	$T_J = T_{\text{case}} + \theta_{JC}P = T_{\text{case}} + P\left(10\frac{^\circ C}{W}\right)$	θ_{JC}: Junction to case thermal resistance, P: power per device (W)
π_E	0.5	Environment factor for space
π_Q	0.25	Quality factor: for Class S parts
π_L	1.0	Learning factor: assumes >2 years production

Table 2. Description of variables for Eq. (4)

Variable	Value	Description
λ_b	$0.0371 = .032\exp(0.345f_{GHz} + 0.0058P_W)$	Base failure rate (assumes 0.4 GHz and 1 W)
π_A	7.6	Application factor for continuous wave devices
π_T	$0.1373 = 0.1\exp\left(-2903\left(\frac{1}{T_J+273}-\frac{1}{373}\right)\right)$	Temperature factor, T_J: junction temperature
	$T_J = T_{case} + \theta_{JC}P = T_{case} + P\left(5\frac{^\circ C}{W}\right)$	θ_{JC}: Junction to case thermal resistance, P: power per device (W)
π_E	0.5	Environment factor for space
π_Q	0.25	Quality factor: assumes Class S parts
π_M	1.0	Matching network factor (input and output)

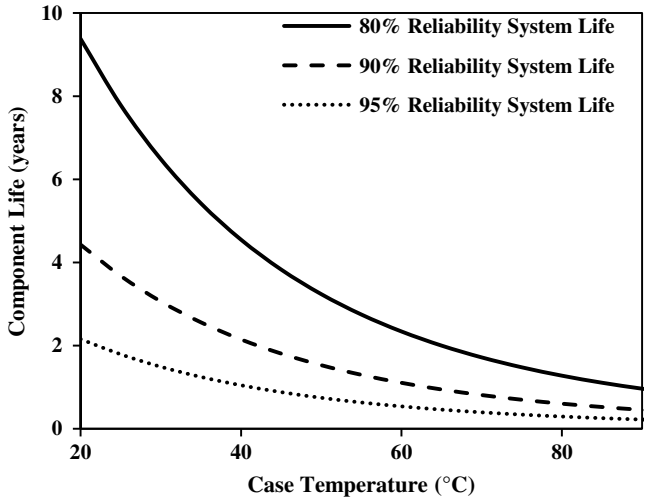

Fig. 1. Transceiver system life in relation to the subsystem operation temperature, showing a significant decrease in reliability with increased operating temperatures.

operation, the heat sink will continue increasing in temperature until the radiator surface is able to dissipate the thermal energy. With a sufficiently large mass of material, the temperature can be kept low. Theoretically assessing 8 min of operation, a high-conductivity metal such as copper at 4.5 mm thick for a 100 cm^2 radiator panel will hold a temperature gain of +15°C (initial temperature= 20°C), for a final temperature of 35°C. The copper heat sink provides excellent thermal management; however, the resulting copper mass is high, at 0.41 kg, which may be unacceptable for the 1.5–2.0 kg per satellite *U* design space. Similar results can be obtained with an aluminum heat sink, resulting in 6.4 mm thick, and 0.17 kg for similar performance

$$mc\frac{dT}{dt} = Q_{in} - \varepsilon\sigma A(T_{surf}^4 - T_{\infty}^4) \tag{6}$$

Phase Change Materials

For any satellite, the thermal control system should be compact, lightweight, and minimize temperature differences between the radiator and electronics being cooled. The alternative to using a large bulky mass is to use a phase change system. Phase change thermal management has the ability to store heat at a lower temperature and dissipate it slowly over time, therefore minimizing oversized radiator designs. A typical system includes a phase change material (PCM) that stores heat at constant temperatures in the transition from solid to liquid and then releases that heat upon resolidifying. Depending on the conditions, supercooling, also known as undercooling, is a notable phenomenon that some PCMs display during the solidification process. Rather than beginning solidification at the freezing point, the material remains liquid until reaching some temperature below this point. Following this is a release of the latent heat of liquefaction, raising the temperature back to the freezing point throughout the remainder of the solidification process. The increment of temperature below the freezing point reached in the liquid state is referred to as the degree of undercooling (Soni et al. 2019). Undercooling commonly takes place when there is no solid phase PCM in the system. For this application, it is not anticipated that all of the PCM will be fully melted. The design of the system should provide sufficient material to hold the desired temperature for a worst case thermal scenario, such as multiple ground station passes in a single orbit. In a design for a heat load scenario 3 standard deviations above the mean duration, more than 99% of the time a fraction (<1/2) of the PCM will be in liquid phase, resulting in minimal undercooling. Also, there is no anticipated forced convection mechanism, and the microgravity environment of on-orbit operations reduces the potential for natural convection to cause a cooling effect.

As PCMs transition phases, it is ideal for the process to occur at the application design temperatures to enhance thermal management. For satellite thermal management, temperatures in the 10°C–40°C range are generally considered, for most components, a safe operational range (Agrawal 1986). Table 3 shows the relevant material properties and options for materials selection with melting points in the 30°C range. Typically, paraffin and hydrated salt systems have been used as PCMs, dating back to the Apollo space program. Paraffin has proven to store heat (~200 J/g) at the solidifying/melting point, however it has low physical density and thermal conductance properties.

The low density leads to less thermal storage per volume and the low thermal conductivity requires more complex thermal conductivity enhancement (TCE) structures to avoid large temperature rises in the PCM. Two popular styles of TCEs are pin fins and blade fins. Pin and blade fins are long round or rectangular cross section structures, respectively, that interlace with the PCM between the hot and cold sides. The function is to minimize the distance traveled

Table 3. Comparison of phase change materials for thermal management (Phase Change Materials Limited 2018)

PCM type	PCM ID	Melting temp (K)	Density (g/mL)	Latent heat (J/g)	Latent heat (J/mL)	Specific heat (J/g · K)	Thermal conductivity (W/m · K)
Hydrated salts	S32	305	1.46	200	292.0	1.91	0.51
	S30	303	1.30	190	247.8	1.90	0.48
	S27	300	1.53	183	280.0	2.20	0.54
Organics	A32	305	0.84	130	109.8	2.20	0.21
	A29	302	0.81	226	183.1	2.15	0.18
	A28	301	0.79	155	122.3	2.22	0.21
	A26	299	0.79	150	118.5	2.22	0.21
Low melting point metals	Ga	302.8	5.91	80.1	*473.3*	0.37	*29.4*
	Cs	301.7	1.80	16.4	29.5	0.24	17.4
	Rb	311.9	1.47	24.7	37.8	0.36	29.3
	Hg	234.1	13.6	11.4	154.4	0.14	8.34

Source: Data from Ge et al. (2013).

by heat through the insulating material, resulting in a lower temperature gradient across the PCM. This enhancement requires an increase in design volume of the heat sink, which also increases mass. Previous research indicated that the best overall performance is achieved by using approximately 8% volumetric fraction of TCE devices (Chen et al. 2016). The performance of a pin-fin TCE based paraffin PCM heat sink was estimated based on 8% fill of aluminum fins, 1.0 mm in diameter and 3.53 mm center spacing. Using steady conduction through the paraffin, the heat sink was expected to produce a temperature change across it of 14.5°C with an overall heat sink thickness of 30 mm and a mass of 70.5 g (37.1 g of PCM). Fig. 1 shows the reliability in change of case temperature from 30°C to 45°C would result in an over 40% drop in mission life.

According to Table 3, gallium is a metallic PCM that has a high latent heat and low melting point similar to these conventional PCMs; however, gallium intrinsically has a much higher density and thermal conductivity. The higher density results in more potential thermal storage, by volume, in the PCM. The thermal conductivity is important in reducing the thermal gradients across the dense material. Due to the low thermal gradients in the material, TCEs would not be necessary in the design. Gallium has the highest latent heat by volume and conductivity of the materials available; meaning, the gallium based heat sink will have the lowest volume of PCM due to the high latent heat by volume and, due to its conductivity, will have the most compact overall design. The higher density will result in a higher mass than the hydrated salts or organic PCM materials; however, small satellites (especially CubeSats) have shown that volume is often a larger constraint than mass, especially when it comes to reliability.

Methods

Phase Change Materials

Gallium has shown to be incompatible with aluminum containers. The gallium rapidly diffuses into the aluminum, resulting in a reduction of structural integrity (Guang and Liu 2009; Ge and Liu 2013). Therefore, the enclosure of a gallium PCM heat sink requires a material selection other than aluminum. The most applicable materials for this research were Inconel 718 and 316 stainless steel. At low temperatures (<400°C), gallium has little interaction with either of these materials (Narh et al. 1998). Both materials are relatively easy to manufacture by selective laser melting (SLM) (Shelton et al. 2019a) and share similar needed material properties to gallium. The materials that are useful for these enclosures have lower conductivity than the gallium [gallium conductivity is 29.4 W/m · K, (Ge et al. 2013), 316 stainless steel is 13.4 W/m · K, and Inconel 718 is approximately 11.7 W/m · K (Bergman et al. 2011)], so TCE structures would inhibit conductivity. Therefore, the only structures required within the heat sink are for structural reasons, preventing vibrational modes while the gallium is molten.

Model Analysis

Several numerical models of PCM heat sinks were constructed. All were assumed one-dimensional models of planar heat transfer through a similar composite wall geometry (Fig. 2). The dimensions shown in Fig. 2 were used for all simulations except with modeling paraffin and hydrated salt, in which the thickness of the PCM was increased by the ratio of latent heat by volume values from 10.7 mm. In all cases, uniform heat flux was applied to the outside of the left wall, conducted through the inner wall, PCM, right heat sink wall, and finally through the radiator material where the right side boundary condition was a radiative condition to a constant environmental temperature. When evaluating on-orbit performance, the environmental temperature was set to 4 K. Due to the low heat flux, the variation in temperature for the radiator laterally away from the heat sink was neglected. Due to the incompatibilities of gallium and aluminum, gallium simulations were assumed with 316 stainless steel or Inconel 718 walls, while paraffin simulations were modeled with aluminum walls. In all cases, the radiator panel was modeled as aluminum.

Lumped Capacitance Model

The lumped capacitance model assumed that the heat sink walls, PCM, and radiator were all of a uniform temperature with the mass and heat capacity combined. Initial calculations indicated that the Biot number for this condition was defined as

$$Bi = \frac{hL_c}{k} \tag{7}$$

where h = effective convection coefficient; L = length; and k = thermal conductivity. For this research, calculating an equivalent

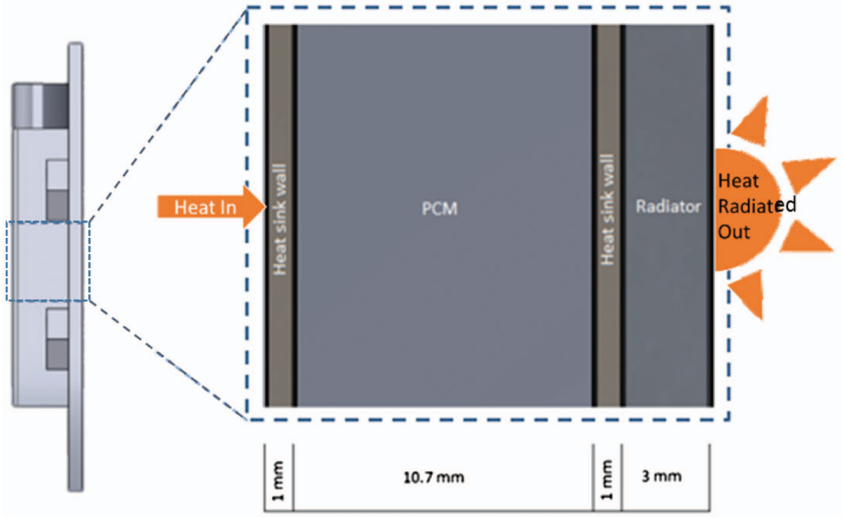

Fig. 2. (Color) Rendering of the gallium heat sink and cross-sectional view of the heat flow through the materials to radiate energy out of the system.

convection coefficient based on the radiative heat transfer (h_r) was from Eq. (8)

$$h_r = \epsilon\sigma(T^2 + T_\infty^2)(T + T_\infty) \tag{8}$$

The Biot number for the gallium filled heat sink, even with conservative assumptions of treating the system as a 15.7 mm thick stainless steel part and calculating the maximum coefficient of heat transfer, was never greater than 0.061. Therefore, the gallium based PCM heat sink could reasonably be treated as lumped capacitance, as the Biot number was less than 0.1 (Bergman et al. 2011), which was verified through finite difference model and experimental results. Conversely, the paraffin based systems required a much thicker layer of PCM with lower conductivity and the lowest Biot number calculated was 0.2, well above the threshold of lumped capacitance models. This calculation ignored the presence of the housing and radiator, calculating only for the paraffin itself, and is therefore highly optimistic but still insufficient for justifying lumped parameter modeling.

In the simulation, after the temperature reached the melting point of gallium, it was held constant while heat storage went into the phase change capacitance. Rather than raising the temperature of the system, the gallium absorbed the energy until fully in the liquid state. Once fully melted, the entire assembly was assumed to increase in temperature again. On removal of the heat source, the left side of the model was assumed to be well-insulated and the right side maintained the radiative condition. As the system cooled, the temperature was held constant at the melting point of the gallium until enough thermal energy had dissipated to resolidify all of the gallium, then continue the cooling process. Supercooling was neglected in the lumped capacitance model, providing a simple yet accurate model. The nonequilibrium solidification model outlined by Soni et al. (2019) showed only a 10% increase (200 out of 2,000 total seconds) in time and 24.3K (8% of the absolute temperature) undercooling temperature required to resolidify the gallium within simulations. This effort would require definition of a boundary between solid and liquid phase material in the PCM, resulting in much more intensive calculations than the lumped capacitance model approach.

Overall, with a low Biot number permitting reasonable accuracy, the lumped capacitance model provides a few benefits. First, it can be used without in-depth knowledge of the system geometry to quickly evaluate designs. The limited resolution of the model requires less information about system specifics and can be used to help design the system. The lumped capacitance model would be completely inadequate for modeling low conductivity systems, such as those using paraffin or hydrated salt PCMs (Bergman et al. 2011).

Finite Difference Heat Equation Model

The finite difference model explored in this research can be much more accurate at evaluating temperature distributions within the system and overall performance; however, it can only be used after a system is designed, unlike the lumped capacitance model. In this model, all of the components were broken up into cells approximately 0.1 mm thick. Boundary conditions were applied similarly to the lumped capacitance model. Non-PCM components were assumed to have constant specific heat, conductivity, and density while the PCM melting was modeled on a cell by cell basis. As the temperature of a given cell reached the melting point of the PCM, it was held constant until enough net heat was stored in the cell to melt the cell's contents fully. At that point, the next cell to the right would reach the melting point and the process would repeat. This process does not result in a level temperature throughout the PCM material, it results in a melt front moving from left to right through the material with a higher temperature gradient behind and a lower gradient in front. Results show temperatures on the heated end of the model can become high before the entire thickness of PCM is melted. The gradient behind the melt front is just under that calculated from the steady state heat equation

$$q'' = k\frac{dT}{dx} \quad or \quad \frac{dT}{dx} = \frac{q''}{k} \tag{9}$$

The gradient is slightly lower (90%–95% of steady state) in this transient condition since some of the energy is being used to heat the already melted PCM and the left wall of the heat sink. Since the conventional PCM has a thermal conductivity of about 1% relative to the gallium, the slope behind the melt front is large, resulting in higher temperatures by comparison. On the right side of the phase change boundary, the gradient is fairly low, as it is limited by the amount of heat removed via radiation on the far right side of the model domain. As mentioned, nonequilibrium solidification for this particular application was unlikely so undercooling was not modeled.

To validate that the model correctly calculates transient conductive heat transfer, a solution for constant properties (Inconel properties were used), constant area, with constant temperature (299 K) on the left boundary and a well-insulated right boundary was calculated and compared to the sum of the first 100 elements of the exact Fourier-series solution, starting from a uniform temperature of 277 K. The two were compared at 6 points in time: 1, 3, 10, 30, 100, and 300 s. Across the 158 spatial points, and these 6 time intervals, the Root-Mean-Square (RMS) error between the approximate analytic solution and the finite difference model solution was 0.0195°C. These differences are negligible in comparison to the 22°C temperature range imposed by the initial and boundary conditions and the bulk of the model can be considered validated. That leaves only the boundary conditions and phase change calculations to be validated. To establish grid independence for the finite difference model, the grid size was reduced by half, from 100 to 50 μm per axial step, and a corresponding decrease in time step from 100 to 25 μs, to maintain solution stability. Over the 3 h simulated run, the RMS change between the two models is 0.11°C on point-to-point comparisons, less than 0.3% of the temperature range represented. The average change was −0.08°C, and the standard deviation of the change was 0.128°C. These negligible changes indicate that the presented results are grid independent.

Experimental Testing

The PCM heat sink, as seen in Fig. 3, was evaluated under two basic sets of conditions: in atmospheric conditions and in vacuum. First, they were tested in air. The PCM device was centered on a 10×10 cm radiator panel. The heated side of the device was insulated using solid Ultem (polyethylimide) (Stratasys, Eden Prairie Minnesota) blocks to minimize convection from the back of the PCM device and radiator. The insulating properties of Ultem also limited conduction. It was designed and printed to fit the heat sinks with 0.5 mm of clearance on the sides and 1 mm of clearance to the heated surfaces and thermocouples. Thermocouples (K type, Minco part number TC40KT40A), with standard accuracy of ±2.2°C and a time constant of 0.6 s were applied to: (1) the heated side of the PCM device; (2) the front radiator face, directly over the PCM device; (3) the back radiator face near the PCM device; and (4) the back radiator face in a corner distant to the PCM device. A similar test was also conducted in a thermal vacuum (TVAC) chamber (< 1.33 MPa), with the only setup change being the application of Z276 Aeroglaze white polyurethane coating to the radiator. This coating is common for spacecraft (Wertz et al. 2011) to enhance

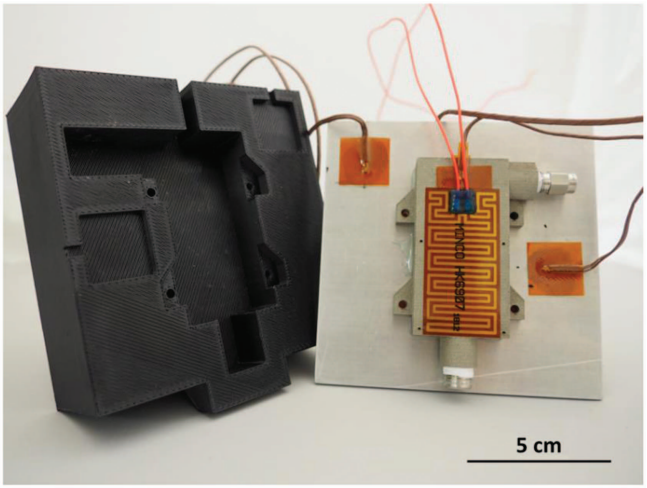

Fig. 3. (Color) Heat sink test setup composed of a gallium PCM within a three-dimensional (3D) printed stainless steel housing. The heat sink has a heater patch on one side and an aluminum radiator panel attached to the other side. The negative Ultem insulator mold and thermocouples installed (3 of 4) are shown.

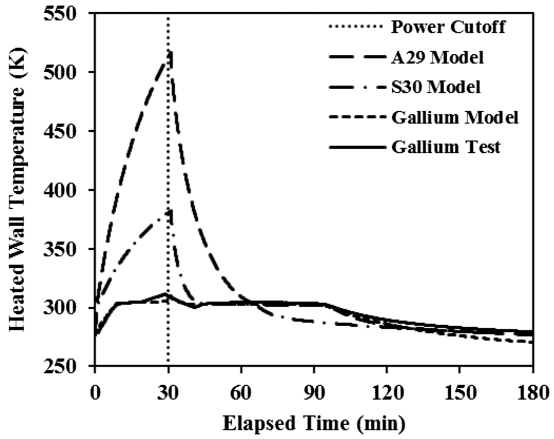

Fig. 4. Comparison of the heated wall temperatures for several modeled PCMs and experimentally measured gallium.

a low solar absorptivity and high thermal emissivity [$\varepsilon > 0.86$, measured at the Air Force Institute of Technology (AFIT)]. Experimentally, the TVAC chamber was set to 260 K, a temperature experimentally attainable. The thermocouples were calibrated using a 2 point method (6 points in ice water at 3.3°C and 5 points in boiling water at 99.89°C, accounting for atmospheric pressure at the time of calibration). This produced a linear correction curve to use the TVAC chamber monitor outputs and correct to an accurate temperature. This correction exhibited a 0.4°C standard deviation from the calibration point data, with an 80% confidence interval for the calibration of 0.2°C. In the region of interest (near 30°C), the linear correction provided approximately a 2.4°C increase from raw output to corrected data.

Results and Discussion

Analysis of the heat sink focused on the following three areas: (1) the benefit of a lumped parameter thermal model for design purposes rather than unnecessary detailed models; (2) the advantages of gallium's high conductivity and density for thermal purposes; and (3) an analytical characterization of the PCM materials.

Model Analysis

Fig. 4 shows the heated wall modeled temperatures of the two conventional PCM materials (A29 and S30) and gallium, along with the experimentally measured hot wall gallium temperature. The conventional and gallium PCMs have very similar melting points at 303 K. For gallium simulations, the fine resolution of finite difference model was used to establish negligible differences from the lumped capacitance model. The models using PCMs other than gallium required the finite difference model, as lumped capacitance was not applicable. Note that the conventional PCM simulations did not have TCE structures built into the model. There is a vertical line indicating the time at which power (heat) was cut off (~30 min). The conventional PCMs did not reach the full liquid phase, as most of the heat was being absorbed by the inside wall of the case and the solidus PCM. Conversely, the gallium PCM heat exchangers were entirely melted and maintained low temperatures. As seen in Fig. 4, the gallium model and experiment have essentially the same thermal profile; however, the measured temperatures began to cool a bit sooner (~3 min). The most critical assumption in this model is the perfectly insulated condition on the right side. The experimental model was insulated but still allowed some heat transfer in that direction by raising the temperature of the insulation.

The A29 and S30 PCMs display the problem of low thermal conductivity for this application. Results have high temperatures near the heat input side of the heat sink. Also, longer times are needed to fully solidify the PCM and fully dissipate the added heat. Fig. 5(a) shows the time-temperature evolution distributed within the S30 PCM heat sink. The temperature gradient in the S30 material is on the order of 8,000 K/m, and while applied over the 10 mm of thickness produces an 80 K increase in temperature at the right side of the model as the PCM is reaching its fully liquid phase. A change in slope at the melting point (303 K) is present. This change in slope is most prominent in the 5–15 min traces, but can be found in the 20–30 min traces also. A radiator temperature increase is present during the 30–35 min range. These results contrast the gallium plot [Fig. 5(b)], in which the temperature gradient on the left side is approximately 130 K/m, resulting in a 1.5 K temperature rise on the right boundary side. The transient temperature is nearly constant across the gallium, as the high thermal conductivity allows for very shallow thermal gradients. This results in a nearly isothermal device. The heated face ($x = 0$) begins at a temperature of 275 K. Applying heat, the first 7–10 min results in a temperature rise to 303 K. Time between 10 and 30 min is the period of gallium melting in the heat sink; the temperature of the heated face rises only 1.5 K. This figure also supports the use of lumped parameter models for initial design of gallium based heat sinks.

Experimental Testing

Fig. 6(a) shows the vacuum testing results of full-melt profiles in the PCM device. The five trials in vacuum show repeatable results with small variations due to initial testing conditions. The power turns on, resulting in a temperature increase until reaching a plateau as the material changes to the liquid phase. Once fully in the liquid phase, the temperature begins to rise again. The power is cutoff to simulate a radio turning off, resulting in the material beginning solidification. The heat begins departing from the system until the PCM is fully solidified. Beyond this point, the heat dissipates

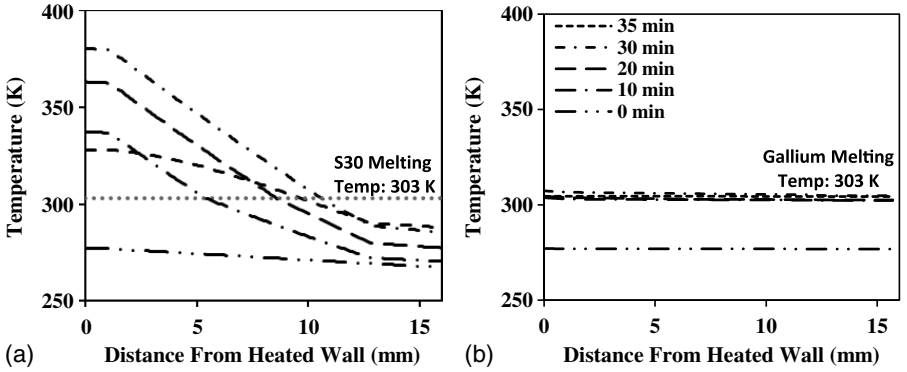

Fig. 5. (a) The temporal evolution of the spatial temperature distribution results in the S30 heat sink; and (b) gallium heat sink.

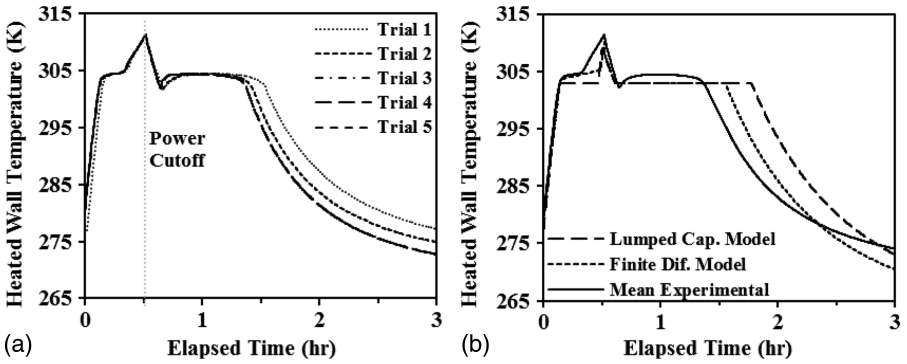

Fig. 6. (a) Inconel full-melt vacuum testing, with 5 separate trials; and (b) average of the 5 trials compared to model results for the heated side in finite difference model one-dimensional (1D) heat equation and lumped parameter models.

through radiation to the chamber walls. Fig. 6(b) shows the overlay of modeling and experimental results. A strong correlation between the model and experimental work is seen. Although sharper transitions are seen in the models, they still incorporate the transitions of phases. The maximum measured temperature is within about 1.3° of prediction. Overall, the experimental performance is seen computationally by both models for the gallium PCM device.

A feature in this data is the supercooling effect near the 0.6 h mark, in which the temperature decreases below the phase transition temperature before rising back above the transition temperature. Before this region, the material is in a fully liquid state until the gallium forms a solid nucleation site. This nucleation site of gallium instantly crystalizes, beginning the crystal growth process to a solid phase. This correlates to the amount of energy lost from the system at that point. As mentioned, the extent of undercooling is important in some applications; however, thermal management for this global time scale is not as strongly affected. It was a small increase in the time required to fully resolidify the PCM. The effect was common in all test articles with short consistent time periods (15–20 min) for the metal housing systems. On average, 1.84 K of supercooling was experienced, with a minimum of 1.51 K and maximum of 2.00 K (standard deviation = 0.19 K), as measured from the average of the plateau region following the supercooling valley. This observed undercooling was much lower (1.84 K, or 0.6% of the absolute temperature) than seen in literature (Soni et al. 2019).

Gallium was also tested in a polymer (Ultem 9085) printed housing to evaluate the finite difference model performance in relation to the systems wall conductivity. However, all polymer printed test articles developed leaks before vacuum testing, so comparable data is not available. In atmospheric testing, the plastic PCM housing showed supercooling temperature drops in the range of 2°C–7°C, with periods over 1 h. In comparison, the metallic housings uniformly had supercooling temperature drops between 1.5°C and 2°C, and durations of 15–20 min. Printed plastic is relatively smooth (Shelton et al. 2019b), having fewer and smaller protrusions into the PCM material that might serve as nucleation sites. Laser scanning micrographs of Ultem [Fig. 7(c)] show a single valley, estimated 60 μm deep, between layers of printed material, while the metals have a significant number of protrusions into the PCM: 25–30 μm high for the Inconel [Fig. 7(b)], and between that size and 70 μm in the stainless steel [Fig. 7(a)]. The topology of the surfaces appear to be a variable to the supercooling behavior, but more study is needed before this conclusion is reached. Since the stainless steel and Inconel surfaces exhibited similar behavior but represent the highest and lowest average roughness, standard statistics such as average roughness do not fully describe the overall surface profile or predict the impacts to supercooling.

Error Analysis

Offsets between experimental and modeled data were calculated. The temperatures were correlated in the experimental data to the nearest time interval in the modeled datasets, as seen in Table 4. Only the first hour of data was used for error analysis in each case.

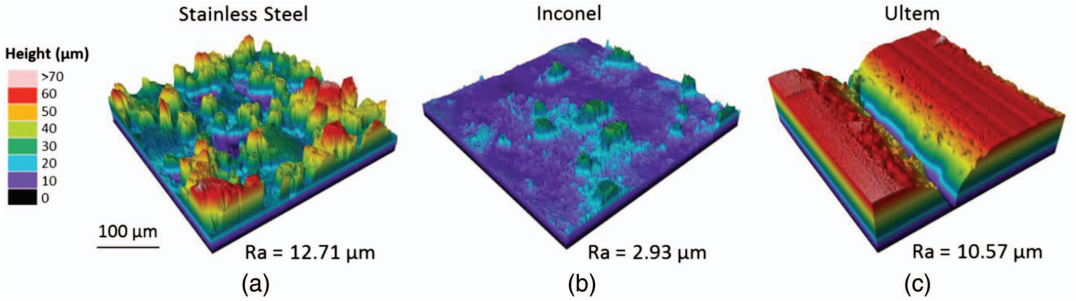

Fig. 7. (Color) Laser scanning micrographs comparing the surface roughness associated with the (a) stainless steel; (b) Inconel; and (c) Ultem 9085 printed housings for the PCMs.

Table 4. Error statistics comparing experimental data to model output (for first hour)

Error characteristic	Test—FDM error (°C)	Test—LC error (°C)
Mean temperature error	1.372	1.844
RMS temperature error	1.763	2.313
Standard deviation of error	1.109	1.397

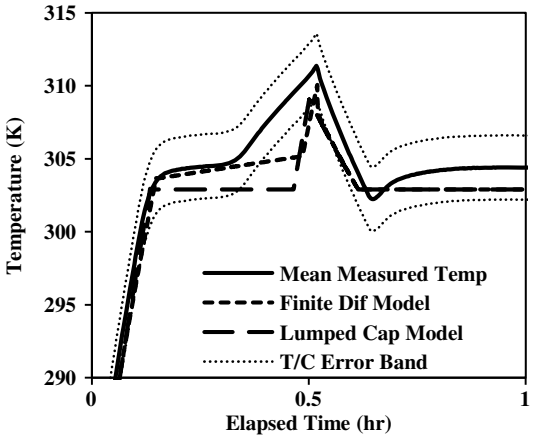

Fig. 8. Associated thermocouple error band of the experimental testing.

After the first hour, other impacts, including the assumption of perfect insulation on five sides in the numerical models, lead to nonrepresentative behavior between the melting and resolidification. This corresponds to 3,600 output points in the model (1 s increments, each representing 10,000 model calculation time steps) and 355 output points in the experimental data (TVAC chamber acquisition at 0.099 Hz). As mentioned, the expected accuracy of the thermocouples is ±2.2°C, both the mean and RMS errors for the finite difference model are within the expected accuracy of the instrumentation, while the lumped capacitance RMS errors are slightly outside the range. Fig. 8 shows the temperature profiles of the lumped capacitance model, finite difference model, and the calibration corrected mean experimental data with thermocouple error bands. Only a few points have the finite difference data outside the thermocouple error band.

Fig. 9 shows the errors directly between both the finite difference and lumped capacitance models and the mean experimental data. Only 15.2% (54/355 points for the finite difference model) and 21.1% (75/355 points for the lumped capacitance model) of

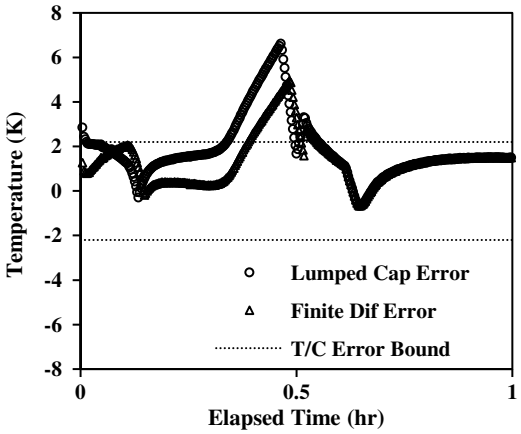

Fig. 9. Temperature error between the mean experimental data and models.

the data points are outside the accuracy limits of the thermocouples used (±2.2°C). The errors are concentrated while the gallium is melting (1/2 > full melt). The error represents a continuous function rather than white noise in the signal, indicating the differences are likely attributable to unmodeled physics. A likely candidate for this behavior is the increase in density as gallium liquefies, leading to an air gap between the heated surface and the gallium during melting. The orientation of the test articles could allow the liquid gallium to move away from the thermocouple location, an increase in thermal resistance not captured in the models. This change in thermal resistance is reflected in the steeper slope at that point in the test data. Offsets in the resolidification period (after 0.5 h), are mostly attributable to the experimental insulator block. This plastic block potentially stored heat and continued radiating after power shutoff, unlike the perfect insulation assumed by the models. Overall, the RMS and mean errors when compared to the experimental data, were close to the accuracy of the thermocouples.

Conclusion

In conclusion, we have used gallium to produce phase change heat sinks. The significant increase in density, coupled with higher mass-specific latent heat, provides a more compact PCM device than traditional materials. The thermal conductivity, higher by 2 orders of magnitude, means a simpler device can be constructed. These properties led to a decrease in the needed volume for the PCM. The higher conductivity also allowed for the temperature change across the device to be nearly an order of magnitude lower

than traditional PCM based devices. A decreased temperature distribution leads to improved application reliability. The high conductivity enabled very simple parametric models, using lumped parameter assumptions, to be used for initial models of the heat sink performance with reasonable accuracy. This combination makes a gallium PCM based heat sink attractive for any system in which high thermal reliability is required.

Data Availability Statement

All data, models, and code used during the study are available from the corresponding author by request. This includes: MatLab code used for simulations; Excel worksheets used for data reduction and design; experimental data including time and temperature data for all tests, both in atmosphere and vacuum; and SolidWorks files for all components unique to this research. Part numbers for commercially sourced material are also available.

Notation

The following symbols are used in this paper:

A = surface area for heat transfer (m^2);
Bi = Biot number, nondimensional value characterizing transient heat transfer (unitless);
C_1 = semiconductor die complexity factor (failures/10^6 h);
C_2 = semiconductor package failure rate (failures/10^6 h);
c = specific heat of a solid or liquid ($J/kg \cdot K$);
h = convective heat transfer coefficient ($W/m^2 \cdot K$);
k = thermal conductivity ($W/m \cdot K$);
L_c = characteristic thickness, length of conductive path (m);
m = mass (kg);
n = number of components (unitless);
P = power (W);
Q = heat flux (W);
q'' = heat flux per unit area (W/m^2);
T = temperature (K);
U = unit of CubeSat volume, $10 \times 10 \times 10$ cm (1 L);
ε = radiative emissivity (unitless);
θ = thermal resistance from semiconductor junction to package case (K/W);
λ_p = device failure rate (failures/10^6 h);
π_A = application factor for calculating device failure rate (unitless);
π_E = environment factor for calculating device failure rate (unitless);
π_L = learning factor for calculating device failure rate (unitless);
π_M = matching network factor for calculating device failure rate (unitless); and
π_Q = quality factor for calculating device failure rate (unitless).

References

Agrawal, B. N. 1986. *Design of geosynchronous spacecraft*. Englewood Cliffs, NJ: Prentice Hall.

Bergman, T. L., A. S. Lavine, F. P. Incropera, and D. P. Dewitt. 2011. *Fundamentals of heat and mass transfer*. 7th ed. Hoboken, NJ: Wiley.

Chen, M., J. Huang, and C. Chen. 2016. "An investigation on phase change device for satellite thermal control." In *Proc., 7th Int. Conf. on Mechanical and Aerospace Engineering*, 100–104. New York: IEEE.

Defense Industry Daily Staff. 2011. "Small is beautiful: US military explores use of microsatellites." Accessed September 26, 2018. https://www.defenseindustrydaily.com/Small-Is-Beautiful-US-Military-Explores-Use-of-Microsatellites-06720/.

Department of Defense. 1991. *MIL-HDBK 217F reliability prediction of electronic equipment*. Washington, DC: Dept. of Defense.

Ge, H., H. Li, S. Mei, and J. Liu. 2013. "Low melting point liquid metal as a new class of phase change material: An emerging frontier in energy area." *Renewable Sustainable Energy Rev.* 21 (May): 331–346. https://doi.org/10.1016/j.rser.2013.01.008.

Ge, H., and J. Liu. 2013. "Keeping smartphones cool with gallium phase change material." *J. Heat Transfer* 135 (5): 054503. https://doi.org/10.1115/1.4023392.

Guang, Y., and J. Liu. 2009. "Corrosion development between liquid gallium and four typical metal substrates used in chip cooling device." *Appl. Phys. A* 95 (3): 907–915. https://doi.org/10.1007/s00339-009-5098-1.

Narh, K. A., V. P. Dwivedi, J. M. Grow, A. Stana, and W. Y. Shih. 1998. "The effect of liquid gallium on the strengths of stainless steel and thermoplastics." *J. Mater. Sci.* 33 (2): 329–337. https://doi.org/10.1023/A:1004359410957.

Phase Change Materials Limited. 2018. "www.pcmproducts.net." Accessed May 15, 2018. http://www.pcmproducts.net/files/plusice_range2011.pdf.

Shelton, T. E., D. J. Stelzer, C. R. Hartsfield, G. R. Cobb, R. P. O'Hara, and C. D. Tommila. 2019a. "Understanding surface roughness of additively manufactured nickel superalloy for space applications." *Rapid Prototyping J.* 26 (3): 557–565. https://doi.org/10.1108/RPJ-02-2019-0049.

Shelton, T. E., Z. A. Willburn, C. R. Hartsfield, G. R. Cobb, J. T. Cerri, and R. A. Kemnitz. 2019b. "Effects of thermal process parameters on mechanical interlayer strength for additively manufactured Ultem 9085." *J. Polym. Test.* 81 (Jan): 106255. https://doi.org/10.1016/j.polymertesting.2019.106255.

Soni, V., A. Kumar, and V. K. Jain. 2019. "A novel solidification model considering undercooling effect for metal based low temperature latent thermal energy management." *J. Storage Mater.* 21 (Feb): 528–542. https://doi.org/10.1016/j.est.2018.12.006.

Wertz, J. R., D. F. Everett, and J. J. Puschell. 2011. *Space mission engineering: The new SMAD*. Hawthorne, CA: Microcosm.